



ELSEVIER

Ultramicroscopy 75 (1999) 251–268

---

---

ultramicroscopy

---

---

# Dynamical direct methods for everyone

W. Sinkler<sup>\*,1</sup>, L.D. Marks

*Department of Materials Science and Engineering, Northwestern University, Evanston, IL 60208-3108, USA*

Received 22 April 1998; received in revised form 28 August 1998

---

## Abstract

Recent work has demonstrated that direct methods, using the minimum relative entropy approach, can be applied to strongly dynamical diffraction from bulk inorganic structures. In the present work, the possibility of using intensity data which is thickness averaged, as for a wedge-shaped specimen, is explored. It is shown that for structures which contain a large number of light atoms, well resolved in projection, use of direct methods with thickness averaged data, combined with limited phase information from high-resolution transmission electron microscopy (HRTEM) can indicate the positions of the light atoms. The possibility of using direct methods from thickness-averaged data allows the use of data from conventional microscopes without fine probe capabilities, and is also of importance for use of direct methods with beam-sensitive samples. © 1999 Published by Elsevier Science B.V. All rights reserved.

---

## 1. Introduction

The most challenging part of solving a crystal structure is often that of specifying an initial set of atomic positions which are reasonably close to the actual structure. Once such an initial set is found, one can employ refinement methods (such as dynamical refinement using multislice, e.g. [1], or Rietveld when powder data are available) to obtain more accurate atomic positions as well as statistical measures of the model's correctness. Current approaches for obtaining direct structure information may be divided into two broad groups. The first are

those which rely on a physical interference effect, such as high-resolution transmission electron microscopy (HRTEM) and holographic methods. In such techniques, interference of diffracted beams preserves phase information in the experimental data. The resulting images may be interpreted directly in terms of crystal structure, or, alternatively, phases can be used in a combined approach with transmission electron diffraction (TED) intensities [2,3]. A second group are statistical direct methods, which are distinguished from HRTEM or holography in that they rely on diffraction intensity data alone. Direct methods systematically approach the problem of assigning the missing phase information to the diffracted beams using probability relationships among them [4]. Sets of phases can be ranked in terms of their overall probability, thereby reducing the solution space of the phase problem. The advantages of direct methods over interference

---

\* Corresponding author.

<sup>1</sup>Current address: Argonne National Laboratory, West, P.O. Box 2528, Idaho Falls, ID 83403, USA. Tel.: +1 208 533 7724; fax: +1 208 533 7863; e-mail: wharton.sinkler@anlw.anl.gov

methods lie in the relative ease of collecting intensity data, as well as in the resolution.

While direct methods have been widely employed in solving crystal structures using single-crystal X-ray diffraction data,<sup>2</sup> dominant dynamical effects in electron diffraction data have prevented their widespread use with TED data. Exceptions to this are recent work on surface reconstructions [5–8], in which the diffraction data originate from approximately a single monolayer of atoms, and are thus largely kinematical [9,10]. Also, work on solving organic structures with TED data was performed as early as the 1960s by Vainshtein [11], but has recently attracted renewed attention, with a number of structures solved over the last several years [12]. The possibility of employing direct methods for structural investigation of inorganics containing heavy elements with electron diffraction has been explored by Fan et al. [13], but only within the kinematical approximation. Because dominant dynamical effects are the rule for such cases, the application of direct methods to electron diffraction data from inorganics requires development of the methods themselves to take dynamical effects into consideration, and a modification of strictly kinematical interpretation. Although prior work in this direction is present in the literature [14], it uses assumptions which are equivalent to nearly kinematical conditions, and which no longer apply for inorganic structures in the thickness range greater than 50 Å. The possibility of routine application of direct methods to solving crystal structures with TED would be of significant value, due to the ease of performing TED, as well as its applicability to samples for which large single crystals cannot be obtained, or in small regions of polyphase materials.

Recently, we have reported the solution of two Ga–In–Sn–O structures using TED and direct methods, combined with limited phase information obtained from HRTEM images [15,16]. In contrast to previous work [13], the direct methods solutions show the clear effect of dynamical changes to the intensities. Dynamical effects resulted in an empha-

sis of the oxygen atom positions in the direct methods solutions, which was particularly useful in combination with both HRTEM and X-ray diffraction, which do not easily detect light atoms. As has been explored elsewhere [16], the usefulness of direct methods in these cases relies on a tendency for the dynamical TED amplitudes to reflect a real-space distribution with atom-like peaks located at the positions of projected columns of light atoms. Direct methods were applied to the diffraction data using the minimum relative entropy algorithm [17,18]. The algorithm restores a real-valued real-space distribution subject to two constraints. Firstly, the Fourier coefficients are constrained to match the diffraction amplitudes, and in addition, the real space map is optimized for consistency with the minimum relative entropy operator, which enforces sharp atom-like peaks and a flat background [17]. The resulting maps clearly showed the oxygen atoms, and provided accurate starting positions for successful refinements using powder neutron and X-ray diffraction [15,19].

The most fundamental issue in using direct methods with dynamical diffraction data is the precise identification of what function direct methods restores. In the case of kinematical diffraction, this is trivially the electrostatic potential  $V(\mathbf{r})$  (or the electron density  $\rho(\mathbf{r})$  for X-rays). In the presence of strong dynamical effects, the diffraction amplitudes are the Fourier moduli  $|\Psi(\mathbf{h})|$  of the exit wave in reciprocal space, which is complex. When direct methods are constrained to restore a *real* function in real space whose Fourier coefficients are identical to the  $|\Psi(\mathbf{h})|$ , this can be neither the exit wave  $\psi(\mathbf{r})$ , nor (because of dynamical effects) the electrostatic potential. As has been shown in previous work [16,20], direct methods in this context can often restore a function resembling the modulus of the Babinet  $|\psi(\mathbf{r}) - 1|$ . While this approximation is not completely general, it provides a satisfactory assessment of the effects of dynamical diffraction in many cases. It can also explain why dynamical effects can be useful in emphasizing the positions of light atoms. Dynamical effects at moderate thicknesses lead quite commonly to an emphasis of light atoms such as oxygen in  $|\psi(\mathbf{r}) - 1|$ , which are in turn preferentially detected by applying direct methods to the dynamical intensity data.

<sup>2</sup> See, for example, The Cambridge Crystallographic Data Centre, at <http://www.ccdc.cam.ac.uk/>.

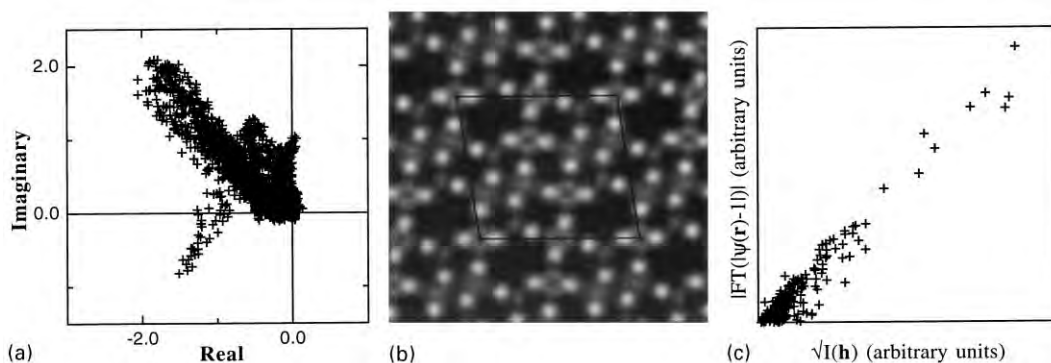


Fig. 1. (a) Argand plot of  $\psi(\mathbf{r}) - 1$  for  $(\text{Ga,In})_2\text{SnO}_5$  [15] along the  $[0\ 1\ 0]$  zone axis direction at  $100\ \text{\AA}$  thickness. All pixels in the unit cell are plotted, based on an exit wave calculation obtained using multislice at  $1\ \text{\AA}^{-1}$  resolution. (b) Plot of  $|\psi(\mathbf{r}) - 1|$ . (c) Plot of the scaling between the Fourier coefficients of  $|\psi(\mathbf{r}) - 1|$  and diffraction amplitudes  $|\Psi(\mathbf{h})|$  for  $100\ \text{\AA}$  thickness (both quantities from multislice).

Fig. 1 provides an explanation of the relationship between the diffracted intensities and  $|\psi(\mathbf{r}) - 1|$ . Fig. 1a shows an Argand diagram for the complex exit wave in real space for  $(\text{Ga,In})_2\text{SnO}_5$ , one of the structures solved using dynamical direct methods [17,21]. In the plot, the real and imaginary part of  $\psi(\mathbf{r}) - 1$  is shown for all of the pixels in one unit cell, calculated using multislice along  $[0\ 1\ 0]$  for a thickness of  $100\ \text{\AA}$ . As can be seen, the function  $\psi(\mathbf{r}) - 1$  is dominated by a large cluster of points with a phase angle of about  $135^\circ$ . In Section 2 below, it is explained that these points are associated with the oxygen  $1s$  channeling eigenstate. Due to the large amplitude of this oxygen eigenstate, the wave at  $100\ \text{\AA}$  has predominantly a single phase (with the exception of a small group of points orientated at approximately  $220^\circ$ , which are associated with one of the cation sites). One therefore can write  $\psi(\mathbf{r}) - 1 \approx |\psi(\mathbf{r}) - 1| \times e^{i\phi}$ , where the constant phase  $\phi$  in the present case is  $\approx 135^\circ$ . Fig. 1b shows a map of  $|\psi(\mathbf{r}) - 1|$  for the present case, and it can be seen that the oxygen atomic positions are the predominant feature of the map. However, from the approximation  $\psi(\mathbf{r}) - 1 \approx |\psi(\mathbf{r}) - 1| \times e^{i\phi}$ , the moduli of the Fourier coefficients of  $|\psi(\mathbf{r}) - 1|$  will scale with the measured diffraction amplitudes (excepting the direct beam). This is because the constant phase is first factored out of the Fourier transform, and then cancels on taking the modulus. The scaling between

the diffraction amplitudes  $|\Psi(\mathbf{h})|$  and  $|\text{FT}\{|\psi(\mathbf{r}) - 1|\}|$  is shown in Fig. 1c for the present case of  $(\text{Ga,In})_2\text{SnO}_5$  at  $100\ \text{\AA}$  thickness [16]. Clearly, the function  $|\psi(\mathbf{r}) - 1|$  satisfies the central constraints of the direct methods approach: its Fourier coefficients scale with the diffraction amplitudes to a good approximation, and it contains sharp atom-like peaks on a flat background. Because of this, the direct methods solution from the experimental amplitudes did resemble Fig. 1b, and was thus directly applicable to solving the oxygen positions in the structure [16]. A similar analysis is expected to hold at intermediate thickness for other structures containing significant numbers of light atoms, arranged in well-resolved columns along the beam direction. This will also be true, for example, in organic structures.

The present work investigates a further extension of the application of direct methods to TED data for the case in which the diffraction data is averaged over thickness, as is characteristic of a wedge-shaped sample. To our knowledge, this is the first time that the effect of such averaging has been considered in direct methods work with TED data. This is a problem of significant practical interest, as thickness averaging can be difficult to avoid in many cases, and it is of importance to consider whether it will dramatically change the result. In addition, it is of interest whether direct methods

can be used with data from a standard selected area (SA) TED experiment to obtain reliable structural information. This would make it possible to employ direct methods with equipment which does not provide a small spot size, or with specimens which cannot be investigated with a condensed beam due to beam sensitivity. As was pointed out previously [16], it is plausible that thickness averaging may actually provide an advantage in some cases. This is because the shallow channeling states associated with light atoms would tend to be accentuated in thickness averaging, whereas the deeper states associated with the heavier atoms would be damped.

In the following section, the theoretical framework for considering thickness-averaging effects in dynamical intensities is presented. The theory is developed using electron channeling theory, supported by comparisons with multislice calculations. Following this, the results of direct methods calculations are presented using both modeled and experimental thickness-averaged intensity. It is found in many cases that direct methods, using data from a simple SA-TED experiment, can provide reliable structural information, with a particular emphasis of light atom positions. The required experimental apparatus is presently widely available in research laboratories and universities. While the direct methods presented here utilize the minimum relative entropy algorithm, the technique is not limited to this algorithm, and similar results should be expected from a variety of direct methods approaches.

## 2. Theory

In employing direct methods with thickness-averaged electron intensity data, the first problem is to identify the function which is likely to be restored, for it is only by doing so that one can understand the results, and assess how dependable the technique will be. An approximation to this problem can be obtained using electron channeling theory [21–25]. In the channeling approximation, the total wave function is expressed as a sum over two-dimensional channeling eigenstates  $\phi_n(\mathbf{R})$ , where  $\mathbf{R} = (x, y)$  is a two-dimensional vector per-

pendicular to the beam direction.

$$\psi(\mathbf{R}, z) = \sum_n C_n \phi_n(\mathbf{R}) \exp\left\{-i\pi \frac{E_n}{E_0} kz\right\}. \quad (1)$$

The sum is over the (normalized) eigenstates, with excitations  $C_i$ . Each eigenstate has a characteristic oscillation frequency as a function of depth ( $z$ ), which is determined by the channeling eigenvalue  $E_n$  ( $E_0$  being the incident beam energy, and  $k = 1/\lambda$ ). For moderate thicknesses and atomic numbers through approximately Fe, the wave corresponding to a single atomic column is dominated by its lowest lying 1s eigenstate (analogous to the atomic 1s state), which has a form resembling the atomic potential [16]. This simplification can be used to make a further approximation [25] for cases in which the atomic columns are well separated in projection, so that the atomic potentials do not strongly overlap. In such cases, one may write

$$\begin{aligned} \psi(\mathbf{R}, z) - 1 \\ = \sum_i C_i \phi_i(\mathbf{R} - \mathbf{R}_i) \left[ \exp\left(-i\pi \frac{E_i}{E_0} kz\right) - 1 \right], \end{aligned} \quad (2)$$

where now the sum is over the  $i$  atomic positions, and the  $\phi_i$  is the 1s channeling eigenfunction for the atomic column centered at  $(x, y) = \mathbf{R}_i$ . The term in the brackets is a unit circle centered at  $(-1, 0)$  in the complex plane. Thus the phase and amplitude of the wave at given  $\mathbf{R}$  and  $z$  describe a circle centered at  $-C_i \phi_i(\mathbf{R})$  in the complex plane. The frequency with which this circle is traversed depends on the channeling eigenvalue  $E_i$  ( $i$  being the closest atom to  $\mathbf{R}$ ). This behavior is illustrated in Fig. 2 using Argand plots of  $\psi(\mathbf{r}) - 1$  calculated by multislice for the  $(\text{Ga,In})_2\text{SnO}_5$  structure at 25 Å thickness intervals between 25 and 200 Å. For 25 and 50 Å, the wave is still dominated by the cations. The three finger-like clusters of points seen in Fig. 2a correspond to the 1s eigenfunctions for Sn, In-Ga and Ga (in order of decreasing phase). Beginning at 75 Å, the broad and slowly rotating cluster of points associated with the shallower oxygen 1s state becomes dominant in the wave. This cluster continues to increase in amplitude and phase through 200 Å thickness, at which point its phase is approximately 180°, and its amplitude is

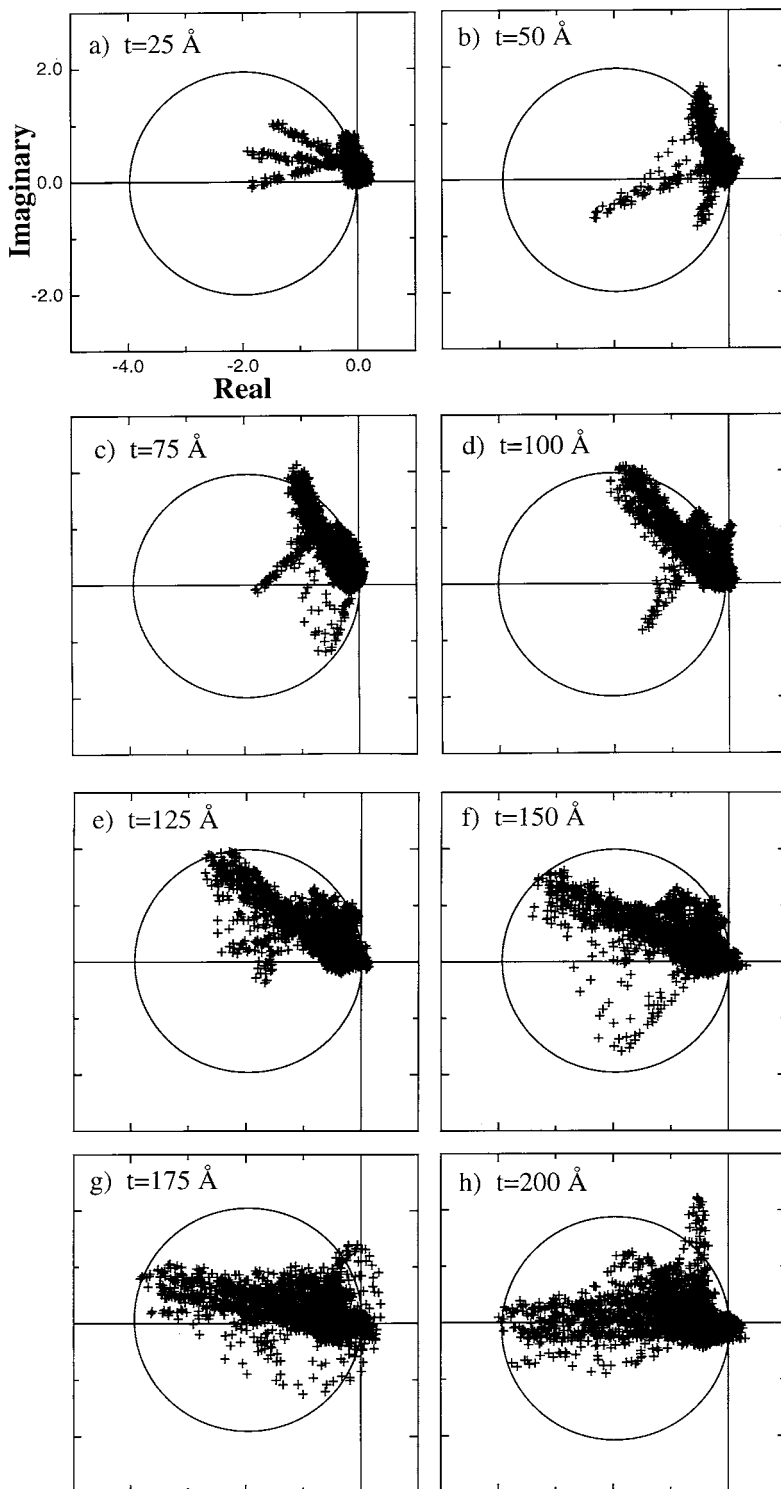


Fig. 2. (a)–(h) Argand plots of  $\psi(r) - 1$  for  $(\text{Ga,In})_2\text{SnO}_5$  along the  $[0\ 1\ 0]$  zone axis direction at 25 Å thickness increments between 25 and 200 Å (from multislice). All figures are to scale.

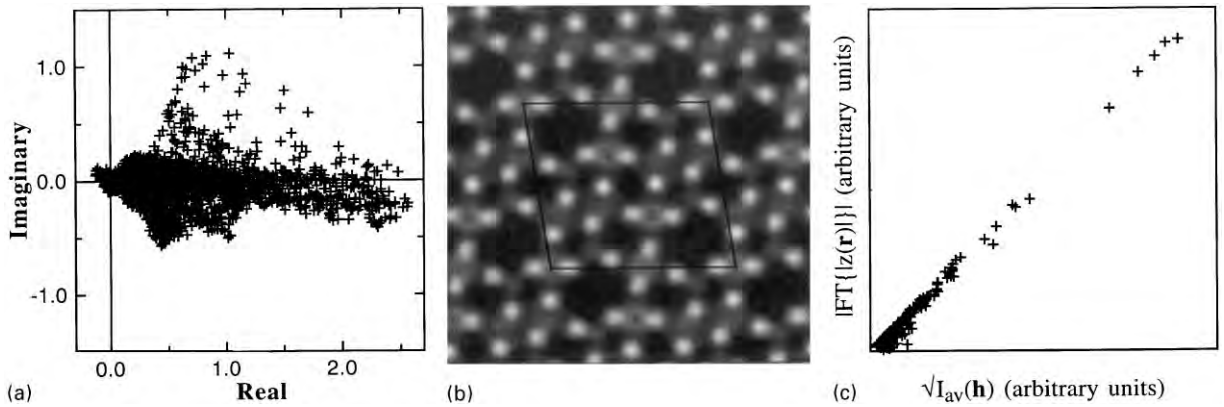


Fig. 3. (a) Argand plot of  $z(\mathbf{r})$  for a single unit cell of  $(\text{Ga,In})_2\text{SnO}_5$ , calculated using  $\Delta\alpha = 2.9^\circ$  and  $\Delta t = 3.16 \text{ \AA}$ . (b) Plot of the real part of  $z(\mathbf{r})$ . (c) Scaling between Fourier coefficients of  $|z(\mathbf{r})|$  and the diffraction amplitudes (from multislice).

approximately 4 (relative to an incident beam of unit amplitude). The circle traced out by the oxygen 1s state with increasing  $z$  is indicated in Fig. 2. From the phase change with thickness, the channeling eigenvalue is approximately  $30 \text{ eV}$ .<sup>3</sup>

Averaging the  $\psi(\mathbf{r}) - 1$  functions over thickness with a factor which cancels the phase of the slowly varying oxygen 1s state would tend to enhance the states corresponding to the oxygen atoms, while decreasing the contribution of the more rapidly varying states for heavier atoms. For the case of a wedge-shaped crystal, one can write this average as

$$z(\mathbf{r}) = \sum_n \exp\{-i(n\Delta\alpha + \pi/2)\} \psi_n(\mathbf{r}), \quad (3)$$

where  $n$  determines the thickness via  $t = n\Delta t$  ( $\Delta t$  being the repeat distance along the beam),  $\Delta\alpha$  is the phase change of the oxygen peak (or another shallow state) per thickness increment  $\Delta t$ , and  $\psi_n(\mathbf{r})$  is the exit wave for thickness  $n\Delta t$ . Averaging the wave according to Eq. (3) was performed using

<sup>3</sup>This is not the same as the 1s channeling eigenvalue obtained for an isolated oxygen atomic column with  $B = 0.3$ , which is  $15.4 \text{ eV}$ . The discrepancy is presumably due to the effect of a small overlap with neighboring column potentials in the multislice simulation. FORTRAN code for calculating s-type channeling eigenvalues can be downloaded at <http://www.numis.nwu.edu/ftp/direct/channeling>.

$\Delta\alpha = 2.9^\circ$  obtained from Eq. (2) using  $E_{1s}$  for oxygen of  $30 \text{ eV}$ ,  $\Delta t = 3.16 \text{ \AA}$  and  $E_0 = 300 \text{ kV}$ . The resulting  $z(\mathbf{r})$  is shown in an Argand plot in Fig. 3a. As can be seen,  $z(\mathbf{r})$  is predominantly real and positive. A plot of the real part of  $z(\mathbf{r})$  is shown in Fig. 3b, and one can see that the averaging has enhanced the peaks at the oxygen sites with respect to those corresponding to the heavier cations. In general, one can expect such averaging to enhance slowly varying shallow states with respect to those which vary rapidly in phase and amplitude. Because the imaginary part of  $z(\mathbf{r})$  is small, and the real part is positive, one has  $\text{Real}(z(\mathbf{r})) \approx |z(\mathbf{r})|$ . In the present case, the appearance of  $|z(\mathbf{r})|$  is not readily distinguishable from Fig. 3b.

If the Fourier coefficients of  $|z(\mathbf{r})|$  were used as input to direct methods, it is reasonable to expect that the oxygen atom positions would be restored as peaks in the solutions. The question thus becomes whether or not the averaged diffraction intensities resemble the modulus squared of  $\text{FT}\{|z(\mathbf{r})|\}$ . Since the averaging has produced a  $z(\mathbf{r})$  which is predominantly real and positive, one has  $|\text{FT}\{|z(\mathbf{r})|\}|^2 \approx |Z(\mathbf{h})|^2$ . From Eq. (3), the latter is given by

$$Z(\mathbf{h})Z^*(\mathbf{h}) = \sum_n |\Psi_n(\mathbf{h})|^2 + 2 \sum_{n < m} \Psi_n(\mathbf{h})\Psi_m^*(\mathbf{h})\cos \Delta\alpha(m - n). \quad (4)$$

In the present work, the intensities for a wedge-shaped sample are approximated by averaging over thickness, which may be justified as shown in Appendix A. The averaged intensities are given by  $I_{av}(\mathbf{h}) = \langle |\Psi(\mathbf{h})|^2 \rangle$ , which is proportional to the first term of Eq. (4). The averaged intensities will thus resemble the Fourier coefficients of  $z(\mathbf{r})$  if the second sum is either small or if it scales with the first sum. The cross terms in the second sum of Eq. (4) will tend to resemble those in the first sum when  $(m - n)$  is small (given that the wave changes slowly as a function of thickness), whereas attenuation via the cosine term will occur if  $(m - n)$  is large. This can be tested by plotting  $|\text{FT}\{|z(\mathbf{r})|\}|$  versus  $\sqrt{I_{av}(\mathbf{h})}$  for a particular case, as is shown in Fig. 3c for  $(\text{Ga,In})_2\text{SnO}_5$ . The figure shows an excellent correlation between  $\sqrt{I_{av}(\mathbf{h})}$  and  $|\text{FT}\{|z(\mathbf{r})|\}|$  in this case. The current analysis and the scaling shown in Fig. 3c rely on two approximations: The first is that  $z(\mathbf{r}) \approx |z(\mathbf{r})|$ , i.e. by appropriate choice of  $\Delta\alpha$  a  $z(\mathbf{r})$  can be constructed which is predominantly real and positive. Secondly, it depends on the second sum of Eq. (4) not deviating strongly from the first. When both approximations are satisfied, the result will be a scaling such as shown in Fig. 3c. Given this scaling, direct methods with input  $\sqrt{I_{av}(\mathbf{h})}$  will very likely result in a solution containing features of  $|z(\mathbf{r})|$ .

In order to test the generality of these characteristics, several additional structures were investi-

gated with regard to the scaling between  $\sqrt{I_{av}(\mathbf{h})}$  and  $|\text{FT}\{|z(\mathbf{r})|\}|$ , and also to determine whether  $|z(\mathbf{r})|$  clearly indicates the positions of light atoms. Figs. 4–6 show the examples of  $\text{Na}_7\text{Nb}_{15}\text{W}_{13}\text{O}_{80}$  [26],  $\text{C}_{32}\text{Br}_{16}\text{CuN}_8$  (copper perbromophthalocyanine) [27] and Ca-doped  $\text{YSr}_2\text{Cu}_2\text{GaO}_7$  [28]. The first two cases clearly showed predominant slowly varying states, which were used to assign  $\Delta\alpha$ . The predominance of these states is related to the large number of well-resolved atomic columns consisting of light atoms. In the case of copper perbromophthalocyanine, the 1s states of the light carbon and nitrogen atoms are the brightest peaks in  $|z(\mathbf{r})|$  (Fig. 5b), while the copper is essentially absent and the bromines are present as fainter, yet broadened peaks (the result of a mixture of 1s and 2s states). In  $\text{Na}_7\text{Nb}_{15}\text{W}_{13}\text{O}_{80}$ , the dominant shallow states are oxygen 1s and Nb/W 2s states, the latter appearing as rings surrounding all projected Nb/W columns in Fig. 4b. In both of the above cases, as also with  $(\text{Ga,In})_2\text{SnO}_5$ , averaging to obtain  $z(\mathbf{r})$ , has accentuated the shallow states, producing a  $z(\mathbf{r})$  which is predominantly real and positive. In these cases, the scaling of  $|\text{FT}\{|z(\mathbf{r})|\}|$  with  $\sqrt{I_{av}(\mathbf{h})}$  is quite good, suggesting that the peaks in  $|z(\mathbf{r})|$  may appear in direct methods solutions.

For the final case of  $\text{YSr}_2\text{Cu}_2\text{GaO}_7$ , the scaling of  $|\text{FT}\{|z(\mathbf{r})|\}|$  and  $\sqrt{I_{av}(\mathbf{h})}$  is considerably poorer. This indicates some degree of breakdown of either of the two approximations in this analysis. In fact,

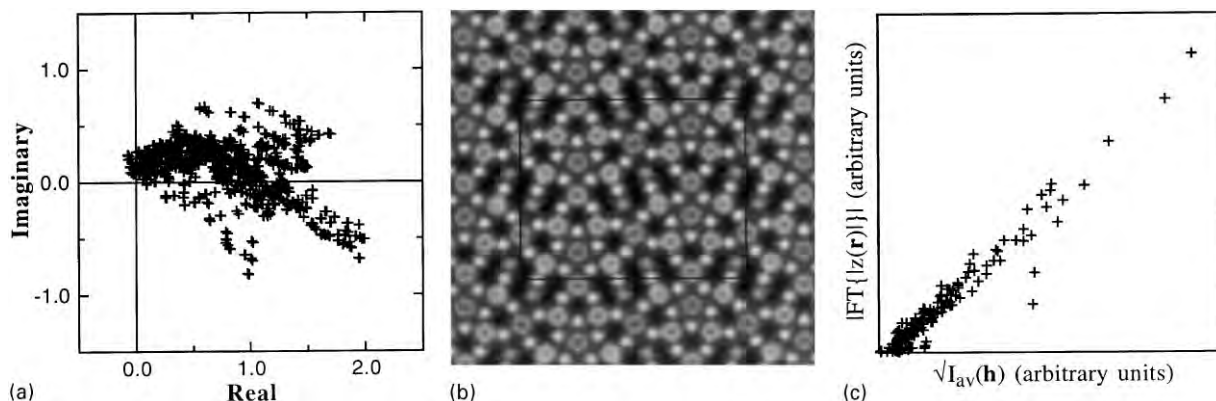


Fig. 4. (a) Argand plot of  $z(\mathbf{r})$  for a single unit cell of  $\text{Na}_7\text{Nb}_{15}\text{W}_{13}\text{O}_{80}$  [26] along  $[1\ 0\ 0]$ , calculated using  $\Delta\alpha = 1.1^\circ$ , and  $\Delta t = 3.92\ \text{\AA}$ . (b) plot of  $|z(\mathbf{r})|$  for one unit cell. The sharp peaks in (b) are positions of pure oxygen atomic columns; Nb/W atomic column positions are recognizable by rings. (c) Scaling between Fourier coefficients of  $|z(\mathbf{r})|$  and the diffraction amplitudes (from multislice).

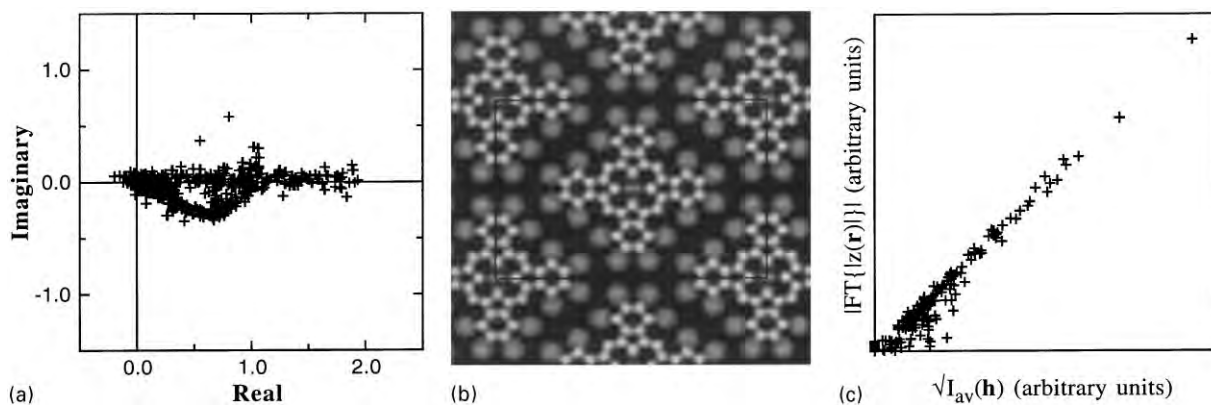


Fig. 5. (a) Argand plot of  $z(\mathbf{r})$  for a single unit cell of  $C_{32}Br_{16}CuN_8$  [27] along  $[0\ 0\ 1]$ , calculated using  $\Delta\alpha = 1.26^\circ$ , and  $\Delta t = 3.76\ \text{\AA}$ . (b) Plot of  $|z(\mathbf{r})|$  for one unit cell. The sharp peaks in (b) are positions of carbon and nitrogen atomic columns, while the bromine columns are visible as very broad, less intense peaks, while the copper at the cell center is nearly extinct. (c) Scaling between Fourier coefficients of  $|z(\mathbf{r})|$  and the diffraction amplitudes (from multislice).

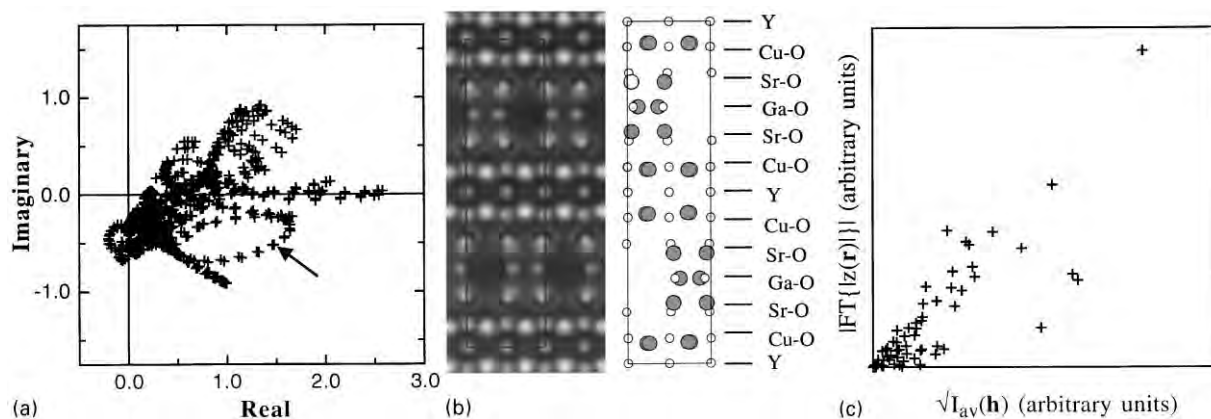


Fig. 6. (a) Argand plot of  $z(\mathbf{r})$  for  $YSr_2Cu_2GaO_7$  [29] along  $[0\ 0\ 1]$ , calculated using  $\Delta\alpha = 1.26^\circ$ , and  $\Delta t = 3.76\ \text{\AA}$ . (b) plot of  $|z(\mathbf{r})|$  for one unit cell, and for comparison a ball-and-stick model of the structure. The sharp peaks in (b) are positions of carbon and nitrogen atomic columns, while the bromine columns are visible as very broad, less intense peaks, and the copper at the cell center is nearly extinct. (c) Scaling between Fourier coefficients of  $|z(\mathbf{r})|$  and the diffraction amplitudes (from multislice).

in this case, the second approximation, i.e. that the second term of Eq. (4) be small, is quite well fulfilled, as was ascertained by plotting  $|\text{FT}\{z(\mathbf{r})\}|$  against  $\sqrt{I_{av}(\mathbf{h})}$  (i.e. using the complex  $z(\mathbf{r})$ ). Rather, it is primarily the first approximation, that  $|\text{FT}\{z(\mathbf{r})\}| \approx |Z(\mathbf{h})|$ , which is violated. In contrast to the three other structures considered, in  $YSr_2Cu_2GaO_7$  structure only a small minority of the projected atomic columns consist purely of

oxygen atoms, and the exit wave is therefore not characterized at intermediate thicknesses of  $\sim 100$  to  $200\ \text{\AA}$  by dominant light-atom s-states with a narrow energy range. The shallow states for this structure occupy a range of energies due to large overlap in the potentials of neighboring atomic columns, for instance at the Ga or Sr columns, both of which have oxygen columns within a distance of less than  $0.6\ \text{\AA}$ . This overlap gives rise to

pronounced dispersion in the two-dimensional band structure, which causes loop-like shapes to appear in the Argand plot. An example of this is indicated by an arrow in Fig. 6a, and it is associated with the overlapping oxygen and gallium columns in the blocking layer (see Fig. 6b). When the low-lying states occupy a continuum of energies, the averaged wave clearly must have a significant imaginary component, and cannot fulfill the requirement of being predominantly real and positive. An additional reason for the poor scaling in the case of  $\text{YSr}_2\text{Cu}_2\text{GaO}_7$  is the relatively low density in the cation columns. There is only one atom per repeat unit along the beam in all cation columns, whereas the pure oxygen columns adjacent to Cu are doubly occupied. The channeling energies for both Ga and Cu are thus relatively low, and the averaging does not strongly attenuate them. This is the source of some rather large positive imaginary values in the Argand plot, many of which are associated with the Cu columns. Based on the results for the  $\text{YSr}_2\text{Cu}_2\text{GaO}_7$  [0 0 1] zone axis, the detection of light atoms using thickness-averaged data will be less effective in structures for which no zone-axis direction exists with a large number of well-resolved atomic columns containing only light elements, and/or when there is poor registry within columns. It will also be negatively affected when low occupation of cation columns gives rise to several closely spaced states at low energy, rather than a single dominant state corresponding to the light atoms.

### 3. Direct methods

Direct methods calculations were performed for simulated data sets for all four structures presented in the previous section, as well as for experimental data sets from the  $(\text{Ga,In})_2\text{SnO}_5$  and  $\text{YSr}_2\text{Cu}_2\text{GaO}_7$  structures. The simulated data sets were obtained by averaging intensities via

$$I_{\text{av}}(\mathbf{h}) = \frac{1}{N} \sum_i |\Psi_i(\mathbf{h})|^2 \quad (5)$$

where  $N$  is the number of repeat distances between 0 and 200 Å, and the  $\Psi_i(\mathbf{h})$  are the wave functions

calculated with multislice for each repeat distance multiple in this interval. Justification for Eq. (5) is provided in Appendix A. The thickness interval used is representative, for example, of a diffraction pattern taken with a 75 nm probe at the edge of a wedge-shaped sample with a wedge angle of  $15^\circ$ . Simulated data sets included all unique beams to  $1 \text{ \AA}^{-1}$  resolution. Although it may be possible to measure intensities beyond this resolution, this will depend on voltage. The  $1 \text{ \AA}^{-1}$  resolution limit was thus chosen as a reasonable practical limit, providing an adequate representation of the features of the exit wave. For obtaining experimental intensities, a Hitachi H9000 microscope was used, operated at 300 kV. In the data set for  $(\text{Ga,In})_2\text{SnO}_5$ , a 100 nm probe was positioned with approximately 40 nm overlap with the specimen. Experimental intensities for  $\text{YSr}_2\text{Cu}_2\text{GaO}_7$  were collected using a 300 nm diameter selected area aperture, positioned approximately  $\frac{1}{3}$  on and  $\frac{2}{3}$  off of the sample. Experimental intensities were measured from microdensitometer scans of through-exposure series on photographic film. The intensities were quantified from the scans using a cross-correlation method [29]. The tilt deviation was small, as indicated by differences between intensities at  $\pm(h, k, l)$  which were in the same range of the measurement errors (about 20%) for both  $\text{YSr}_2\text{Cu}_2\text{GaO}_7$  and  $(\text{Ga,In})_2\text{SnO}_5$ .

The direct methods calculations were performed using the minimum relative entropy approach described elsewhere [17,18]. The calculations assumed that a limited number of low-resolution image phases were available. Where the phases were not taken from actual experimental HRTEM images (the cases of  $(\text{Ga,In})_2\text{SnO}_5$  and  $\text{YSr}_2\text{Cu}_2\text{GaO}_7$ ), simulated images for Scherzer defocus and a thin sample ( $\approx 30 \text{ \AA}$ ) were used to assign phases for a number of low-angle beams (approximately 10% of the total data set). The criteria in choosing which phases to fix were based on the strength of the image Fourier coefficient, and a limitation on the spatial frequency to below  $0.45 \text{ \AA}^{-1}$  (short of the Scherzer limit for both experimental and calculated images). For such reflections the phase of  $\text{FT}(|\psi(\mathbf{r}) - 1|)$  tends to be stable as a function of crystal thickness [16], so that the image phase information (the same as

Table 1

Image phases used for  $(\text{Ga,In})_2\text{SnO}_5$ . The phases were taken from an experimental HRTEM image, and represent 18 of 305 unique reflections. All phases are in agreement with  $\text{FT}\{|z(\mathbf{r})|\}$

$h,l$	Image phase
4, -1	180
0,3	180
2, -1	180
4,2	180
2,0	360
5,0	360
3, -1	180
1,3	180
1, -2	180
3, -3	180
1, -1	360
1, -3	360
3,0	180
1,1	180
4, -2	180
0,4	360
2, -3	360
3, -2	360

$\text{FT}(|\psi(\mathbf{r}) - 1|)$  at low spatial frequency) is likely to be characteristic of the function  $|z(\mathbf{r})|$ . The phases used are listed for each structure in Tables 1–4, where they are compared with the corresponding phases in  $|z(\mathbf{r})|$ . As can be seen, there is nearly perfect agreement between the image phase information and  $\text{FT}\{|z(\mathbf{r})|\}$  except in the case of  $\text{YSr}_2\text{Cu}_2\text{GaO}_7$ .

In performing the direct methods calculations on the thickness-averaged diffraction data, normalization of the root intensity (amplitude) data was performed using

$$|U(\mathbf{h})| = |F(\mathbf{h})| \cdot W(\mathbf{h}) / \langle |F(\mathbf{h})| \rangle,$$

in which  $W(\mathbf{h})$  is a window function designed to improve the self-consistency of peaks in the solutions with the minimum relative entropy operator, and  $\langle |F(\mathbf{h})| \rangle$  is the expectation value of  $|F(\mathbf{h})|$ . Under the assumption of randomly located atoms,  $\langle |F(\mathbf{h})| \rangle$  is given by  $\{\sum_i f_i^2\}^{1/2}$ , where the sum is over the atomic scattering factors for all atoms in the unit cell.

It was reproducibly found in direct methods using thickness-averaged dynamical intensity data

Table 2

Image phases used for  $\text{Na}_7\text{Nb}_{15}\text{W}_{13}\text{O}_{80}$ . The phases were obtained from a calculated HRTEM image, and represent 20 of 305 unique reflections. All phases are in agreement with  $\text{FT}\{|z(\mathbf{r})|\}$

$h,k$	Image phase
2,6	180
0,8	180
4,6	180
6,2	360
2,0	180
4,4	360
0,2	180
6,5	180
6,6	180
6,4	180
2,2	180
6,0	180
4,3	360
4,5	180
4,1	360
2,3	360
2,7	180
6,1	180
2,1	360
2,5	360

that the use of very large Debye–Waller factors in the normalization led to better prediction of phases in terms of finding peaks representative of the  $|z(\mathbf{r})|$  maps shown in the previous section. Under the present conditions, Debye–Waller factors corresponding to an rms spread of approximately 0.8 Å for heavy cations and 0.3 Å for the light atoms was found to produce good results for all structures investigated. This can be explained by the tendency for the peaks in the wave, and thus in  $|z(\mathbf{r})|$ , to broaden as the thickness increases, due to the increasing importance of shallow 2s and p states which unlike the 1s states are not maximal at the atomic positions. A good example of this can be found in Fig. 5b, which shows  $|z(\mathbf{r})|$  for copper perbromophthalocyanine. The peaks at the bromine atomic positions have a breadth (full-width at half-maximum) of nearly 2 Å, while those at the carbon atoms are about 0.8 Å in breadth. This contrasts with potential peak widths for the structure model used in the multislice calculation, which were approximately 0.9 Å for the bromines, and 0.7 Å for

Table 3

Image phases used for  $C_{32}Br_{16}CuN_8$ . The phases were obtained from a calculated HRTEM image at Scherzer defocus, and represent 18 of 191 unique reflections

$h,k$	Image phase
4,8	360
3,5	180
7,1	360
1,9	360
3,7	360
6,4	360
4,4	180
6,0	180
5,5	360
1,11	360
0,8	180
5,7	180
6,6	360
2,4	360
2,8	180
5,1	360*
1,7	360
0,10	360

A single phase in disagreement with  $FT\{|z(\mathbf{r})|\}$  is marked with an asterisk.

Table 4

Image phases used for  $YSr_2Cu_2GaO_7$ . The phases were obtained from an experimental HRTEM image, and represent 5 of 57 unique reflections

$h,k$	Image phase
1,1	360
2,0	360*
4,0	180
6,0	180*
10,0	360

Phases in disagreement with  $FT\{|z(\mathbf{r})|\}$  are marked with an asterisk.

the carbon atoms. The inclusion of large Debye–Waller terms in the normalization mimics this dynamically induced broadening of the atomic column peaks in  $|z(\mathbf{r})|$ , and is thus beneficial towards restoring the features of  $|z(\mathbf{r})|$ . The fact that the additional 2s- and p-type states dominate more quickly for heavier elements supports the use of a Z-dependent correction to the thermal factors. Fig. 7 is a plot of the total normalization factor

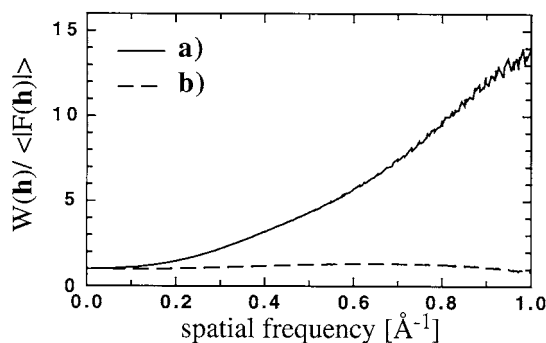


Fig. 7. Plots of the total normalization factor  $W(\mathbf{h})/\langle|F(\mathbf{h})|\rangle$  versus spatial frequency  $|\mathbf{h}|$  for copper perbromophthalocyanine: (a) using large thermal parameters; (b) using standard small thermal parameters.

$W(\mathbf{h})/\langle|F(\mathbf{h})|\rangle$  used for the example of perbromophthalocyanine as a function of spatial frequency  $\mathbf{h}$ . This is also compared with a normalization using Debye–Waller factors of  $0.3 \text{ \AA}^2$ , or  $0.06 \text{ \AA}$  rms vibrational amplitude.

The details of the direct methods algorithm used will not be described here, as they have been discussed in detail in previous publications [17,18,20]. Subsequent to normalization of the amplitudes as described, two consecutive direct methods calculations were performed for each structure. An initial run was performed, after which it was observed which beams among the strongest in the data set had strongly defined phases (having the same phase in all of the top 10 solutions). These were then assigned fixed phases, and the process was repeated a second time. This two-step procedure was found to be beneficial particularly in the cases of perbromophthalocyanine and  $Na_7Nb_{15}W_{13}O_{80}$ , which have rather large projected unit cells, and thus contain a large number of beams.

Fig. 8a–d shows direct methods solutions for all four structures considered using simulated data. The solutions shown represent the top solutions in terms of the figure of merit (FOM) [17,18] in all cases except for  $YSr_2Cu_2GaO_7$ , for which the second-ranked solution is shown. The top solution for  $YSr_2Cu_2GaO_7$  was discounted due to its strongly inhomogeneous appearance (it had only two strong peaks in the unit cell). The solutions are consistent with the analysis of Section 2 for all but the case of

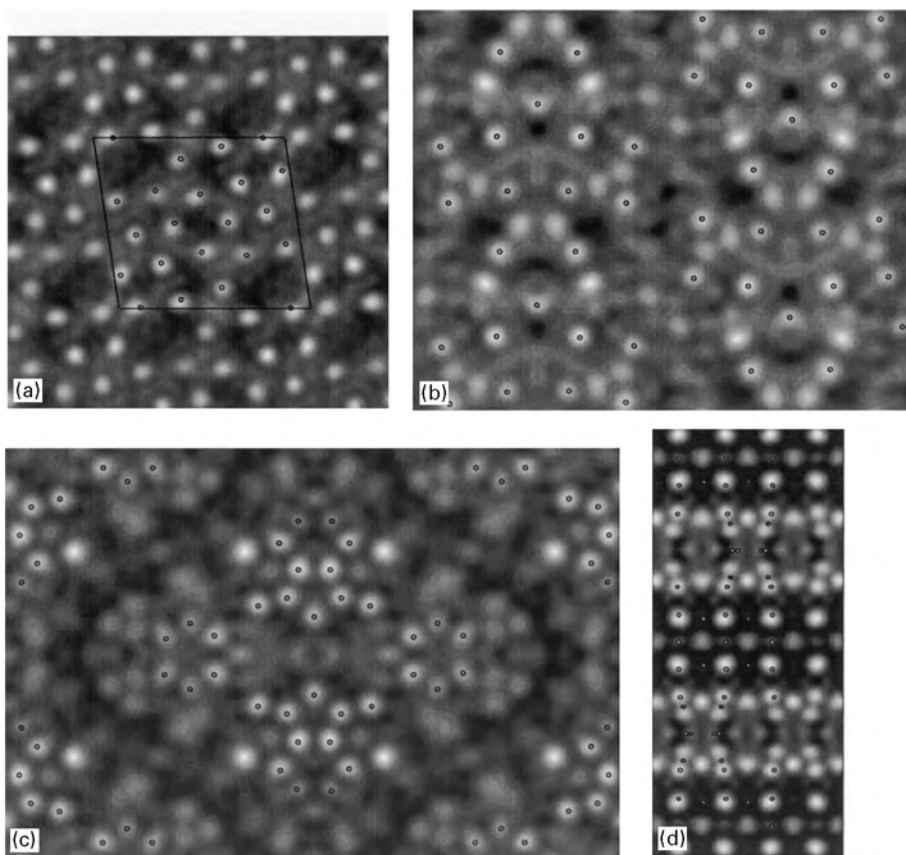


Fig. 8. Direct methods solutions obtained using averaged intensities for thicknesses between 0 and 200 Å. (a)  $(\text{Ga,In})_2\text{SnO}_5$ , with rings marking positions of all oxygen atomic columns. (b)  $\text{Na}_7\text{Nb}_{15}\text{W}_{13}\text{O}_{80}$ , with rings marking positions of the 46 (of 52 total) oxygen atomic columns which are present as peaks in the solution. (c)  $\text{C}_{32}\text{Br}_{16}\text{CuN}_8$ , with rings marking the positions of the 64 (of 80 total) light atom positions present as peaks in the solution. (d) For  $\text{YSr}_2\text{Cu}_2\text{GaO}_7$ .

$\text{YSr}_2\text{Cu}_2\text{GaO}_7$ . They consistently reflect the low-lying channeling states seen in the  $|z(r)|$  plots, and are therefore a good guide to the positions of light atoms in the structure. This is particularly true for the case of  $(\text{Ga,In})_2\text{SnO}_5$ , as should be expected based on the excellent scaling between the input amplitude data and the Fourier coefficients of  $|z(r)|$ . For the larger structures, perbromophthalocyanine and  $\text{Na}_7\text{Nb}_{15}\text{W}_{13}\text{O}_{80}$ , the predominant peaks are those of the light atoms, while additional peaks are located at the bromine (perbromophthalocyanine) and W–Nb ( $\text{Na}_7\text{Nb}_{15}\text{W}_{13}\text{O}_{80}$ ) sites. In the case of perbromophthalocyanine, 64 carbon and nitrogen sites are recognizably associated with peaks in the

direct methods solution, out of a total of 80 sites. For  $\text{Na}_7\text{Nb}_{15}\text{W}_{13}\text{O}_{80}$ , 46 of a total of 52 oxygen atomic columns are indicated by peaks in the direct methods solution. For both structures there are a number of additional peaks in the direct methods solutions, most of which are associated with heavier atoms in the structure (as well as in  $|z(r)|$ ). Thus, for example, there are a few peaks in Fig. 8c which correspond to bromine atoms, and in Fig. 8b some features appear at the locations of the ring-like features marking W/Nb sites in Fig. 4b. Because these are all features of  $|z(r)|$ , and given the good scaling between the diffraction intensities and  $|z(r)|$  in these cases, the appearance of these features

corresponding to shallow states in the exit wave is not surprising. While the respective structures are not necessarily solvable without further effort using Fig. 8b and c, the direct methods solutions would clearly be of significant benefit to solving the structures. Provided the additional availability of HRTEM images, with indications of where the heavy cations of the structures are located, it is likely that the correct structural model could readily be developed.

Fig. 8d presents the second-ranked direct methods solution for the case of  $\text{YSr}_2\text{Cu}_2\text{GaO}_7$ , using simulated diffraction intensities. As can be seen, a number of the strongest peaks in the direct methods solution correspond to projected atomic columns. Nevertheless, the solution does not bear much resemblance to the function  $|z(r)|$  presented in the previous section. The solution also does not emphasize light atoms or shallow channeling states in any systematic way. While the solution might be useful in solving the structure, the approach of Section 2 cannot be used to predict the dependability of direct methods for this case.

In addition to modeled diffraction intensities, direct methods was performed using experimental diffraction intensities for both  $(\text{Ga,In})_2\text{SnO}_5$  and  $\text{YSr}_2\text{Cu}_2\text{GaO}_7$ . The direct methods solutions are shown as Fig. 9a and Fig. 9b. The solutions bear a reasonable resemblance to those obtained with modeled data in both cases. In the case of  $(\text{Ga,In})_2\text{SnO}_5$ , the oxygen positions are the most prominent peaks of the direct methods solution. Additional weaker peaks are located at two of the tin positions (arrows), and two of the gallium positions (double arrows). The exact nature of the result will depend on the precise weighting with respect to thickness, as well as the details of the direct methods calculations (for example the normalization employed). Nevertheless, the sensitivity of direct methods to the light atom positions which is evident in Fig. 9a is in general agreement with expectations based on the analysis of Section 2 for the  $(\text{Ga,In})_2\text{SnO}_5$  structure. In the case of  $\text{YSr}_2\text{Cu}_2\text{GaO}_7$ , the direct methods solution using experimental data has several features in common with the solution from modeled data (Fig. 8d) as well as with the structure. There are strong maxima near the atomic columns in the Sr–O layers, and

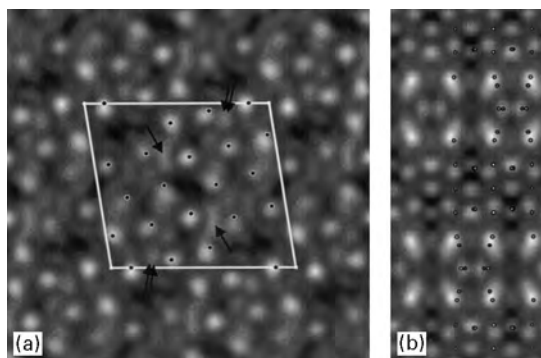


Fig. 9. (a) Direct methods solution obtained using experimental thickness-averaged electron intensity data from  $(\text{Ga,In})_2\text{SnO}_5$ . The solution shows peaks at all oxygen atomic positions (dots) as well as fainter peaks at two tin positions (single arrows) and two gallium positions (double arrows). (b) Direct methods solution from experimental thickness-averaged intensity data from  $\text{YSr}_2\text{Cu}_2\text{GaO}_7$ . Overlay shows a ball-and-stick model of the structure.

weaker maxima in the Ga–O layers, also corresponding well with the mixed oxygen-gallium atomic columns. In the yttrium layers, the yttrium has a weak maximum, and there is a spurious maximum between the yttrium columns. In contrast to the solution from modeled data the Cu–O layers show only weak maxima near the Cu columns, and slightly stronger maxima near the pure oxygen columns. Altogether, it is possible that the direct methods solution for  $\text{YSr}_2\text{Cu}_2\text{GaO}_7$  might be useful for solving the crystal structure. However, it must be pointed out that the reliability of the present technique in this case is uncertain, because there is as yet no systematic means of obtaining a prediction concerning probable features of the direct methods solution. This contrasts with the other three cases considered, in which it is at least probable that a simple interpretation based on sensitivity to light atom positions provides a simple and reasonably reliable basis for interpreting the direct methods solutions.

#### 4. Discussion

The present work develops a methodology for determination of crystal structures using

thickness-averaged electron diffraction intensities combined with limited HRTEM image information. It has been shown in both modeled and experimental cases that thickness-averaged intensity data can be used for direct methods calculations to indicate probable atomic positions. Once these initial positions are obtained, subsequent refinement techniques can be used to improve the accuracy of the structure data, as well as to confirm the correctness of the structure. The technique has particular sensitivity to light atom positions, and is viable in structures which contain a large number of light atoms, located in well-resolved atomic columns parallel to the incident beam. For such cases (which include many organic structures), the direct methods result is sensitive to light atom positions. This is a consequence of a narrow and shallow channeling energy band corresponding to the light atom 1s states. These states are accentuated both using thickness-averaged intensity data, as well as in single-thickness data from thicknesses in the range of 100–200 Å at conventional accelerating voltages [16]. In contrasting cases for which there is significant overlap of neighboring atomic columns, the direct methods result becomes difficult to predict. Dependable atomic resolution using direct methods in such cases may perhaps be obtained by taking extreme precautions to gather data from a very thin region ( $< 50$  Å thickness). An additional possibility for less tractable structures such as  $\text{YSr}_2\text{Cu}_2\text{GaO}_7$  would be to use single-thickness data in a more general Fourier restoration scheme, in which the solutions are complex (see e.g. Ref. [30]). It may be possible to use such an approach together with limited phase information from a through-focus series to restore the complex exit wave. This alternative is currently being developed.

The possibility of obtaining structural information using thickness-averaged intensity data means that the use of dynamical direct methods is not restricted to data collected using microscopes which are designed to provide an electron probe in the nanometer range. Data for direct methods can be obtained using conventional or older high-resolution instruments, and all experimental data used in the present work was collected using a standard HRTEM instrument with a probe size on the order of 100 nm. This may be particularly useful, because

a single experimental session on a high-resolution microscope can suffice to collect all data used for a direct methods structure determination: Subsequent to obtaining high-resolution images (for image phases), a diffraction through-exposure series can be collected from the same sample area used for the imaging.

While most of the details of the technique have been discussed in the above Sections 2 and 3, three points of practical importance should be mentioned. The first concerns the collection of the data, and in particular the restrictions on sample thickness. In addition to the data sets employed to obtain Fig. 9a and Fig. 9b above, a third data set was collected from the  $[010]$  zone axis of  $(\text{Ga},\text{In})_2\text{SnO}_5$  using a 300 nm diameter selected area aperture, overlapping the specimen by 200 nm. The direct methods result using this data did not reveal the oxygen atomic positions, while that taken using a 100 nm condensed beam, overlapping the sample by 40 nm did (see Fig. 9a). Based on the five times greater beam–specimen overlap, the failure of the selected area data to provide approximate oxygen atomic positions was likely due to excessive specimen thickness (based on a  $20^\circ$  wedge angle, the maximum thickness exceeded 1000 Å). For thicknesses in this range, inelastic effects become dominant, and the channeling approximations concerning the exit wave – that it is essentially flat with peaks at the positions of atomic columns – break down. In general, the thicknesses for which direct methods should work along the lines presented here are closer to the range of 100–200 Å, which are characteristic of a sample with a small wedge angle ( $< 20^\circ$ ), using a probe–specimen overlap on the order of 50 nm. This is nevertheless easily achieved using virtually any microscope manufactured within the last 20 years.

A second aspect of practical importance is the adjustment made to the diffraction amplitude normalization to account for dynamical effects in the data. This represents a first approximation towards modifying the direct methods calculation when working with dynamical data. As pointed out above, the large thermal factors used for normalization mimic the Z-dependent broadening of peaks in the wave which occurs through excitation of 2s- and p-type channeling eigenstates. Use of this

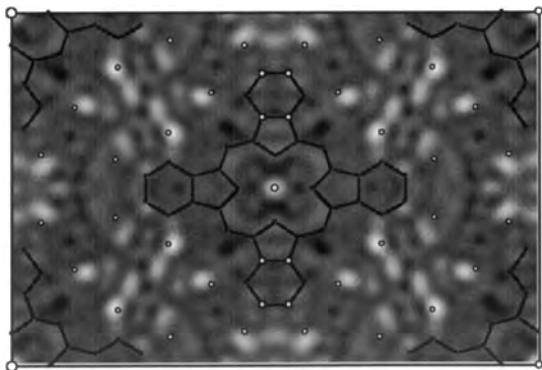


Fig. 10. Direct methods solution from modeled thickness-averaged diffraction intensities for copper perbromophthalocyanine. Overlay shows ball-and-stick model of the structure, with large dots at the cation positions. The solution was obtained using a standard normalization with small thermal parameters corresponding to 0.06 Å rms vibration amplitude.

normalization led to the most faithful reproduction of the function  $|z(\mathbf{r})|$ , including the predominance of peaks at the positions of light atoms (see Fig. 8a–c). It is interesting to note that use of the standard normalization which would be used with kinematical data (Fig. 7, curve b) results in solutions which are not reminiscent of  $|z(\mathbf{r})|$  but nevertheless may contain peaks at atomic positions. This is shown in Fig. 10 for the case of copper perbromophthalocyanine. While this direct methods solution differs strongly from that shown as Fig. 8c, the peaks in Fig. 10 show a reasonable correlation with the cation positions in the structure. The emphasis of the cation positions can be understood based on the fact that the total integrated size of the peaks at the bromines in  $|z(\mathbf{r})|$  (Fig. 5b) is nearly twice as large as that at the light atoms, in spite of the light atoms being stronger in terms of their peak amplitude. Fig. 10, which compared to Fig. 8c is a less faithful restoration of the sought-after  $|z(\mathbf{r})|$ , is consistent with the enhanced sensitivity towards real-space distributions containing broader peaks which results from a flatter normalization. This is because the flat normalization produces a reciprocal space distribution in which the reflections at high angle are damped, and the real-space features must therefore be relatively broad. Under these constraints, the direct methods calculation thus

provides a solution which contains fewer peaks, but in which these peaks are the largest ones in  $|z(\mathbf{r})|$ . In contrast, a normalization using large thermal factors increases the relative strength of large-angle beams and results more consistently in locating most of the peaks in  $|z(\mathbf{r})|$ , thereby emphasizing the light atom positions.

Finally, it may be noted that all of the examples treated in the present work are from centrosymmetric projections. This is not a constraint of the present direct methods algorithm, but derives solely from the use of initial phases taken from HRTEM images. For centrosymmetric projections the image phases are limited to 0 and  $\pi$ , which thus eliminates the significant error in image phases from non-centrosymmetric projections. As pointed out above, the use of image phases is indispensable in dynamical direct methods. Image phases for non-centrosymmetric projections may be used provided that care is taken to statistically assess and if possible reduce their error. An additional alternative for non-centrosymmetric structures is to employ the image phases as a fixed constraint in the first several cycles or projections, and subsequently (because of their potential for introducing error) allow them to vary in the final cycles.

## 5. Conclusions

The present work has investigated the possibility of applying direct methods to thickness-averaged electron diffraction intensities. Direct methods were applied to both modeled and experimental electron diffraction intensities from several known crystal structures. It is found that in structures containing a large proportion of columns of light atoms, aligned along the incident electron beam and well separated from neighboring columns, direct methods is able to indicate the positions of the light atom columns. A theoretical framework for understanding the application of direct methods to thickness-averaged dynamical diffraction intensities has been developed, using electron channeling theory. The work provides the basis for using conventional TEM equipment without fine probe capabilities to obtain diffraction data for use

towards solving crystal structures with direct methods.

**Acknowledgements**

The authors would like to acknowledge helpful discussions with E. Landree and E. Bengu. Collaborations with K.R. Poeppelmeier, T.O. Mason and J.D. Jorgensen are gratefully acknowledged. We also wish to thank D. Ko and D.D. Edwards for providing samples. The project was made possible through support from the National Science Foundation (DMR 91-20000) through the Science and Technology Center for Superconductivity.

**Appendix A**

Considering the case of a wedge-shaped sample, in the one-dimensional geometry shown in Fig. 11, the exit wave can be expressed as

$$\psi(x) = \sum_g \Psi_g(mx) \exp(2\pi i g x) \exp(-2\pi i m x / \lambda), \quad (A.1)$$

where  $\Psi_g(t)$  is the waves Fourier coefficient at  $g$  for thickness  $t$ ,  $\lambda$  is the electron wavelength, and  $m = \tan(\beta)$  (see Fig. 11). From Fig. 11 the thickness at position  $x$  is equal to  $mx$ . Eq. (A.1) thus considers the wave at  $x$  as identical to that of a planar sample with thickness  $mx$ , for which the incident wave is out of phase (with respect to that arriving at  $x = 0$ ) by  $-2\pi m x / \lambda$ . If one sets:

$$W_g(u) = FT\{\Psi_g(mx) \exp(-2\pi i m x / \lambda)\} \quad (A.2)$$

(in which the FT is taken with respect to the variable  $x$ , and the  $\Psi_g$  are all equal zero for  $x$  outside of the aperture interval  $x = 0 \dots x_{max}$ ), one then has from the Fourier transform of Eq. (A.1):

$$\Psi(u) = \sum_g \delta(u - g) * W_g(u) \quad (A.3)$$

in which  $*$  denotes convolution. By assuming that all  $W_g(u)$  are well localized around the reflection at wavevector  $g$ , one can integrate over a small region

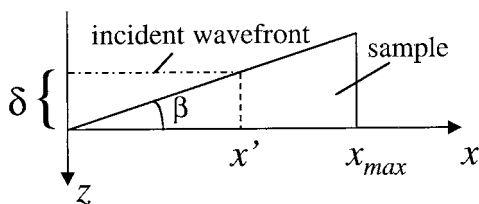


Fig. 11. Schematic diagram of a wedge-shaped sample with wedge angle  $\alpha$ . The phase difference of the incident wave at  $x'$  relative to that at  $x = 0$  is  $2\pi\delta/\lambda$ . Using  $m = \tan(\alpha)$  this is  $2\pi m x / \lambda$ . The aperture or beam width extends from  $x = 0 \dots x_{max}$ .

$\Delta u$  around  $g$  to obtain

$$I_g \approx \int_{\Delta u} |W_g(u)|^2 du \quad (A.4)$$

for the intensity of the reflection at  $g$ . This is the same as calculating the intensities for planar samples and averaging, as is done in Eq. (5) to approximate the scattered intensity from a wedge-shaped sample. One can show this from Parseval's theorem. Assuming that the region  $\Delta u$  includes all the intensity scattered from within the aperture corresponding to the beam  $g$ , one has

$$\begin{aligned} \int_{\Delta u} |W_g(u)|^2 du &= \int_A |\Psi_g(mx) \exp(-2\pi i m x / \lambda)|^2 dx \\ &= \int_A |\Psi_g(mx)|^2 dx \end{aligned} \quad (A.5)$$

in which  $A$  indicates the area  $0 \dots x_{max}$  contained within the aperture. The assumption that the  $W_g(u)$  are localized around the reflection at  $g$  is critical to this approximation. In order to justify this, one needs detailed information concerning the function  $\Psi_g(t)$ . The channeling approximation is well suited for this problem because of its analytical thickness dependence. For a one-dimensional primitive unit cell, containing a single column of atoms, one has a form analogous to Eq. (2)

$$\psi(x) = 1 + C_1 \phi_1 \left\{ \exp\left(-i\pi \frac{E_1}{E_0} kt\right) - 1 \right\} \quad (A.6)$$

in which  $\phi_1(x)$  is the 1s channeling eigenfunction, and  $E_1$  is the corresponding eigenvalue. This gives

Table 5

Characteristic spread of diffracted beams due to a local variation of thickness as a function of wedge angle and channeling eigenvalue. Values are in ( $\text{\AA}^{-1}$ )

Energy (eV)	10	30	100	200
Angle (deg)				
5	0.000087	0.00026	0.00087	0.0017
10	0.00017	0.00052	0.0018	0.0035
15	0.00026	0.00080	0.0027	0.0053
30	0.00057	0.00172	0.0058	0.012

$\Psi_g(t)$  as

$$\Psi_g(t) = \delta(g) + C_1 \Phi_1(g) \left\{ \exp\left(-i\pi \frac{E_1}{E_0} kt\right) - 1 \right\}. \quad (\text{A.7})$$

Inserting this into Eq. (A.2) along with an aperture function  $A(x)$ , which is equal to 1 inside the aperture and zero outside, one obtains

$$W_g(u) = C_1 \Phi_1(g) \left\{ \left[ \delta\left(u - \left(\frac{E_1}{2E_0} km + km\right)\right) - \delta(u - km) \right] \frac{\sin \pi x_{\max} u}{\pi u} \exp(i\pi u x_{\max}) \right\}. \quad (\text{A.8})$$

Here  $C_1 \Phi_1(g)$  is proportional to the electron scattering factor, and is assumed to be nearly constant close to the reciprocal lattice vector  $g$ . The intensity variation around this reciprocal lattice vector due both to the aperture and the wedge shape of the sample is given as a function of  $u$  by the term in the curved brackets. From Eq. (A.8), the sample thickness variation within the aperture introduces a spread in  $W_g(t)$  which is of the order  $\Delta u = (E_1/2E_0)km$ . In a more general channeling scheme starting from Eq. (1) of the main article,  $E_1$  is replaced by  $\Delta E$ , which is the total energy spread between the deepest and shallowest excited channeling states. The magnitude of  $\Delta u$  for representative values of  $E_1$  and the wedge angle  $\alpha$  are given in Table 5 for 200 kV accelerating voltage. Considering that the distance between reflections is the inverse of the lattice parameter, the values of  $\Delta u$  would amount to a significant portion of the dis-

tance between reflections only in extreme cases in which the wedge angle is  $30^\circ$ , the channeling eigenvalue is 200 eV and the lattice parameter is several tens of  $\text{\AA}$ . Channeling eigenvalues exceeding 200 eV occur only for elements heavier than approximately Mo, aligned in perfect columns along the beam. This supports the validity of Eq. (5) for approximating the diffracted intensity from a wedge-shaped sample.

## References

- [1] J. Jansen, D. Tang, H.W. Zandbergen, H. Schenk, *Acta Crystallogr. A* 54 (1998) 91.
- [2] T.E. Weirich, R. Ramlau, A. Simon, S. Hovmöller, X. Zou, *Nature* 382 (1996) 144.
- [3] H.W. Zandbergen, S. Andersen, J. Jansen, *Science* 277 (1997) 1221.
- [4] M. Woolfson, H.-F. Fan, *Physical and Non-Physical Methods of Solving Crystal Structures*, Cambridge University Press, Cambridge, 1995.
- [5] C. Collazo-Davila, L.D. Marks, K. Nishii, Y. Tanishiro, *Surf. Rev. Lett.* 4 (1997) 65.
- [6] C.J. Gilmore, L.D. Marks, D. Grozea, C. Collazo-Davila, E. Landree, R.D. Twisten, *Surf. Sci.* 381 (1997) 77.
- [7] E. Landree, L.D. Marks, P. Zschack, C. Gilmore, *Surf. Sci.* 408 (1998) 300.
- [8] L.D. Marks, R. Plass, D.L. Dorset, *Surf. Rev. Lett.* 4 (1997) 1.
- [9] Y. Tanishiro, K. Takayanagi, *Ultramicroscopy* 27 (1989) 1.
- [10] L.D. Marks, T.S. Savage, J.P. Zhang, R. Ai, *Ultramicroscopy* 38 (1991) 343.
- [11] B.K. Vainshtein, *Structure Analysis by Electron Diffraction*, Pergamon Press, Oxford, 1964.
- [12] D.L. Dorset, *Structural Electron Crystallography*, Plenum Press, New York, 1995.
- [13] H.-F. Fan, S.B. Xiang, F.H. Li, Q. Pan, N. Uyeda, Y. Fujiyoshi, *Ultramicroscopy* 36 (1991) 361.
- [14] W.F. Tivol, *Acta Crystallogr. A* 51 (1995) 708.
- [15] W. Sinkler, L.D. Marks, D.D. Edwards, T.O. Mason, K.R. Poepelmeier, Z. Hu, J.D. Jorgensen, *J. Solid State Chem.* 136 (1998) 145.
- [16] W. Sinkler, E. Bengu, L.D. Marks, *Acta Crystallogr. A* 54 (1998) 591.
- [17] L.D. Marks, E. Landree, *Acta Crystallogr. A* 54 (1998) 296.
- [18] L.D. Marks, E. Bengu, C. Collazo-Davila, D. Grozea, E. Landree, C. Leslie, W. Sinkler, *Surf. Rev. Lett.* 5 (1998) 1085.
- [19] D.D. Edwards, T.O. Mason, W. Sinkler, L.D. Marks, K.R. Poepelmeier, 1998, in preparation.
- [20] W. Sinkler, L.D. Marks, *Materials Characterization* (1998), in press.
- [21] M.V. Berry, *J. Phys. C* 4 (1971) 697.
- [22] A. Tamura, Y.H. Ohtsuki, *Phys. Stat. Sol.* 62 (1974) 477.

- [23] F. Fujimoto, *Phys. Stat. Sol.* 45 (1978) 99.
- [24] K. Kambe, *Ultramicroscopy* 10 (1982) 223.
- [25] D. Van Dyck, M. Op de Beeck, *Ultramicroscopy* 64 (1996) 99.
- [26] Marinder, Sundberg, *Acta Crystallogr. A* (1984).
- [27] D.L. Dorset, W.F. Tivol, J.N. Turner, *Acta Crystallogr. A* 84 (1992) 562.
- [28] J.T. Vaughey, J.P. Thiel, E.F. Hasty, D.A. Groenke, C.L. Stern, K.R. Poepelmeier, B. Dabrowski, D.G. Hinks, A.W. Mitchell, *Chem. Mater.* 3 (1991) 935.
- [29] P. Xu, G. Jayaram, L.D. Marks, *Ultramicroscopy* 53 (1994) 15.
- [30] J.R. Fienup, *J. Opt. Soc. Am.* 4 (1987) 118.